



HIGH-ENERGY NEUTRINOS FROM SOURCES IN CLUSTERS OF GALAXIES

KE FANG^{1,2} AND ANGELA V. OLINTO³¹ University of Maryland, Department of Astronomy, 1105 PSC, College Park, MD 20742, USA² Joint Space-Science Institute, College Park, MD 20742, USA³ Department of Astronomy & Astrophysics, Kavli Institute for Cosmological Physics, The University of Chicago, Chicago, Illinois 60637, USA*Received 2015 November 11; revised 2016 June 27; accepted 2016 July 1; published 2016 August 26*

ABSTRACT

High-energy cosmic rays can be accelerated in clusters of galaxies, by mega-parsec scale shocks induced by the accretion of gas during the formation of large-scale structures, or by powerful sources harbored in clusters. Once accelerated, the highest energy particles leave the cluster via almost rectilinear trajectories, while lower energy ones can be confined by the cluster magnetic field up to cosmological time and interact with the intracluster gas. Using a realistic model of the baryon distribution and the turbulent magnetic field in clusters, we studied the propagation and hadronic interaction of high-energy protons in the intracluster medium. We report the cumulative cosmic-ray and neutrino spectra generated by galaxy clusters, including embedded sources, and demonstrate that clusters can contribute a significant fraction of the observed IceCube neutrinos above 30 TeV while remaining undetected in high-energy cosmic rays and γ rays for reasonable choices of parameters and source scenarios.

Key words: astroparticle physics – galaxies: clusters: general – neutrinos

1. INTRODUCTION

The IceCube Observatory observed the first high-energy astrophysical neutrinos (Aartsen et al. 2013a, 2013b, 2013c). The all-flavor diffuse neutrino flux is reported to be $\Phi_\nu = 2.06 \times 10^{-18} (E_\nu/10^5 \text{ GeV})^{-2.46} \text{ GeV}^{-1} \text{ cm}^{-2} \text{ sr}^{-1} \text{ s}^{-1}$ for the energy range of $25 \text{ TeV} < E_\nu < 1.4 \text{ PeV}$ (Aartsen et al. 2015). Searches for small-scale anisotropies from the three-year IceCube data do not see any significant clustering or correlations (Aartsen et al. 2015). The origin of these high-energy neutrinos remains unclear (Murase 2015).

Accretion of gas during the formation of the large-scale structure can give rise to mega-parsec scale shocks that accelerate high-energy cosmic rays (Miniati et al. 2000; Ryu et al. 2003), and even ultra-high-energy cosmic rays (UHECRs) if the medium around the shocks contain heavy nuclei (Inoue et al. 2007). Numerical simulations (Hong et al. 2014; Vazza et al. 2014; Miniati 2015) also suggest the possibility of stochastic particle acceleration in large-scale structures, though the flux level of cosmic rays depends on the Mach number and the location of shocks (Vazza et al. 2014).

Powerful sources harbored in the galaxy clusters can also accelerate particles to high energies. Many plausible candidate sources have been proposed in the literature, including steady sources like active galactic nuclei (AGNs; e.g., Stecker et al. 1991; Winter 2013; Dermer et al. 2014; Murase et al. 2014), and transients like gamma-ray bursts (see Mészáros 2006 for review), fast-spinning newborn pulsars (Blasi et al. 2000; Fang et al. 2012, 2013), magnetars (Arons 2003; Murase et al. 2009), and blazar flares (Farrar & Gruzinov 2009).

Clusters are famously known as cosmic-ray reservoirs, due to their ability to confine cosmic rays with turbulent magnetic fields up to cosmological time (Völk et al. 1996; Berezhinsky et al. 1997, also see Brunetti & Jones 2015 for a recent review). Hence the accelerated cosmic rays have a good chance to interact with the intracluster medium (ICM), leading to the production of secondary neutrinos and γ rays. A cosmic-ray reservoir scenario is favored to explain the absence of detection of neutrinos above a few PeV, especially around the Glashow resonance at 6.3 PeV. This is because rather than an otherwise

mysterious stop in the cosmic-ray spectrum, a “cosmic-ray reservoir” scenario naturally introduces a spectral softening caused by the faster escape of the higher-energy cosmic rays in a magnetized source environment.

Many analytical and semi-analytical works were conducted to calculate these secondary fluxes (Dar & Shaviv 1995; Völk et al. 1996; Berezhinsky et al. 1997; de Marco et al. 2006; Murase et al. 2008; Wolfe et al. 2008; Murase et al. 2013). However, most of the analytical approaches adopted an overly simplified modeling of the ICM by assuming both uniform gas distribution and uniform magnetic field. Colafrancesco & Blasi (1998) took into account the density profile and mass function of galaxy clusters, yet they still assumed a uniform magnetic field within each cluster and the same cosmic-ray diffusion length for all groups of clusters with different masses. Numerical propagation of cosmic rays in more realistic three-dimensional cluster magnetic fields were explored by Rordorf et al. (2004) and Kotera et al. (2009), but the studies were limited to neutrinos from a single type of cluster.

Numerical modeling of the non-uniform gas distribution and magnetic field structure is crucial in an environment like the ICM because both duration and location of the confinement of the charged particles impact the interaction rate, and thus an accurate computation of the neutrino production. Moreover, although massive clusters could be brighter cosmic-ray and neutrino sources, they are far less common than medium-sized clusters. It is thus unclear how the mass and redshift dependence of cluster number density would impact the total neutrino spectrum. It is also unknown which group of clusters would dominate PeV cosmic rays and thus be more relevant for the detected neutrinos. The latter point is also important for revealing the possibility of pinpointing sources with the increasing statistics of IceCube as well as future experiments (Ahlers & Halzen 2014; Fang & Miller 2016).

Bechtol et al. (2015) pointed out that new studies of the blazar flux at gamma-rays above 50 GeV result in a lower residual non-blazar component of the extragalactic gamma-ray background. This puts a tight constraint on neutrino sources that are transparent to gamma-rays (Murase et al. 2016),

especially those that produce neutrinos through hadronuclear (pp) interactions (as in galaxy clusters; Kotera et al. 2009). However, this constraint is drawn based on the assumption that the pp scenario has a E^{-2} spectrum extended below ~ 10 TeV, which is not necessarily valid for all source types. For example, particles accelerated by fast-spinning newborn pulsars (Blasi et al. 2000; Fang et al. 2012, 2013) can have a spectrum index less than two, and cosmic rays accelerated in the AGN (Dermer et al. 2012; Murase et al. 2012) can present a cutoff at low energies due to the confinement of the source environment.

In this paper, we investigate high-energy cosmic rays and neutrinos from clusters, by numerically propagating cosmic rays down to TeV in galaxy clusters with a wide range of masses and redshifts. We limit the uncertainties of our results with a more realistic modeling of the ICM gas and the turbulent cluster magnetic field than some of the previous works, and by adopting the mass accretion rates, cluster baryon fraction, and halo mass function as constrained by cosmological observations.

We report the integrated cosmic-ray and neutrino spectra from the entire cluster population in two scenarios:

1. the *accretion shock scenario*: cosmic rays are accelerated by the cluster accretion shocks and injected at the outskirts of clusters; and
2. the *central source scenario*: cosmic rays are accelerated by sources at the centers of the clusters.

Our results demonstrate that neutrinos from cluster accretion shocks could contribute $\lesssim 20\%$ of the IceCube flux; however, if bright astrophysical sources inside the galaxy clusters can accelerate particles with an injection spectrum index below two, clusters could reproduce both the spectrum and flux of IceCube neutrinos above 30 TeV, while remaining consistent with the measurements of high-energy cosmic rays and γ rays.

2. MODELS

In this section, we lay out the models used in our work. We first review the particle acceleration in clusters in Section 2.1, then examine the diffusion and confinement of cosmic rays in the turbulent cluster magnetic field in Section 2.2. We calculate the neutrino production in a single cluster in Section 2.3, and discuss the formalism used to integrate the source contributions in Section 2.4.

2.1. Cosmic-Ray Acceleration

Charged particles can get accelerated by large-scale shocks induced by cluster accretion activities, or (and) produced by the powerful sources harbored inside the clusters. Below, we discuss the two scenarios accordingly.

The spatial scale of the accretion shocks can be estimated by the virial radius of the host cluster. For a cluster with a mass of $M = M_{15} \times 10^{15} M_{\odot}$ at redshift z , the size of the accretion shock is

$$\begin{aligned} r_{\text{sh}} &\approx r_{\text{vir}} = \left(\frac{3M}{4\pi \Delta_{\text{vir}}(z) \rho_m(0)} \right)^{1/3} \\ &= 2.6 M_{15}^{1/3} \left(\frac{\Delta_{\text{vir}}(0)}{\Delta_{\text{vir}}(z)} \right)^{1/3} \text{ Mpc}, \end{aligned} \quad (1)$$

where $\Delta_{\text{vir}}(z) \approx (18\pi^2 + 82x - 39x^2)/(x + 1)$ with $x = \Omega_M(z) - 1$ is the virial overdensity with respect to the

mean matter density (Hu & Kravtsov 2003). For simplicity, the cosmological term $\Delta_{\text{vir}}(0)/\Delta_{\text{vir}}(z)$ will be ignored in the analytical estimations below (for reference, $\Delta_{\text{vir}}(0)/\Delta_{\text{vir}}(1) \approx 1.6$).

The typical velocity of accretion shocks should be comparable to the free-fall velocity (Inoue et al. 2007; Murase et al. 2008), which reads $v_{\text{sh}} \approx \sqrt{GM/r_{\text{sh}}} = 1300 M_{15}^{1/3} \text{ km s}^{-1}$. The acceleration time in a strong shock can be estimated by $t_{\text{acc}} = 20 D_{\text{sh}}/v_{\text{sh}}^2$ (Kang et al. 1997; Inoue et al. 2007), assuming a quasi-parallel shock. Note this time can be much shorter for oblique shocks with more general magnetic field angles (Jokipii 1987). Strong accretion shocks are expected at the outskirts of clusters (Vazza et al. 2014). Taking the Bohm limit, the diffusion coefficient of the cluster shock reads $D_{\text{sh}} = r_L c/3$, where $r_L = E/ZeB$ is the Larmor radius of a cosmic-ray particle with energy E and charge Z in a magnetic field B . In a shock with field strength $B = 1 B_{-6} \mu\text{G}$, the acceleration time for a particle to reach $E_{\text{cr}} = 10^{18} E_{\text{cr},18} \text{ eV}$ would be $t_{\text{acc}} = 1.3 E_{\text{cr},18} M_{15}^{-2/3} B_{-6}^{-1} Z^{-1} \text{ Gyr}$. On the other hand, the maximum time cosmic rays stay in the shocks due to diffusive escape is $t_{\text{esc}} \approx r_{\text{sh}}^2/6 D_{\text{sh}}$ (Inoue et al. 2007). $t_{\text{acc}} = t_{\text{esc}}$ thus sets the maximum energy that cosmic rays can be accelerated to

$$E_{\text{cr,max}} = 2.8 \times 10^{18} M_{15}^{2/3} Z B_{-6} \text{ eV}. \quad (2)$$

The energy budget of high-energy cosmic rays is determined by the accretion rate of the cluster. The mass accretion rate of halos can be described by a fitting function $\langle \dot{M} \rangle = 42(M/10^{12} M_{\odot})^{1.127} (1 + 1.17z) E(z) M_{\odot} \text{ yr}^{-1}$ (McBride et al. 2009), with $E(z) = \sqrt{\Omega_m(1+z)^3 + \Omega_{\Lambda}}$. Note that in this work we take $\Omega_m = 0.308$, $h = 67.8$ (Planck Collaboration et al. 2015) and assume a flat universe.

The kinetic energy of the accretion shocks is $L_{\text{acc}} = f_b GMM/r_{\text{sh}}$, with $f_b = 0.13(M/10^{14} M_{\odot})^{0.16}$ being the average baryon fraction of galaxy clusters (Gonzalez et al. 2013). If a fraction $f_{\text{cr}} = 1\% f_{\text{cr},-2}$ of this energy is converted into cosmic rays, the luminosity of cosmic rays from accretion shocks is then

$$L_{\text{cr}} = 2.0 \times 10^{44} M_{15}^{1.95} f_{\text{cr},-2} \text{ erg s}^{-1}. \quad (3)$$

Note that the cosmic-ray luminosity of a cluster is highly dependent on the cluster mass.

Particles accelerated in high-energy sources inside the clusters can have very different spectra and energetics depending on the source types. In general, E^{-2} spectrum would be expected from diffusive shock accelerations, but harder spectra are possible when the particle energy is converted from the electromagnetic energy of the sources, for example, in pulsar magnetospheres (Arons 2003), or in reconnection processes (Guo et al. 2014). Besides, an interplay between the acceleration and dissipation processes at the acceleration site could also lead to a hard injection spectrum (Dermer et al. 2012; Murase et al. 2012). Murase et al. (2016) and Bechtol et al. (2015) demonstrated that a pp scenario with a E^{-2} spectrum normalized to the IceCube datapoint at ~ 10 TeV would overproduce γ rays above the flux of the non-blazar component of the isotropic γ -ray background. In this work, we will instead consider the case of an injection spectrum index equal or smaller than two, but normalized to the IceCube datapoint at 30 TeV (which is about three times lower than that at 10 TeV). Specifically, in Section 3, we focus on a

benchmark case of an injection spectrum $dN/dE \propto E^{-1.5}$ and maximum energy $E_{\max} = 50$ PeV. We discuss the effects of different choices of dN/dE and E_{\max} in Section 4.

2.2. Cosmic-Ray Diffusion

Galaxy clusters are known as efficient containers of cosmic rays (Völk et al. 1996; Berezhinsky et al. 1997). Depending on the particle's Larmor radius r_L and the field's coherence length l_c , the propagation of cosmic rays in the cluster turbulent magnetic field can be divided into semi-diffusive ($r_L > l_c$) and diffusive ($r_L \ll l_c$) regimes (Kotera & Lemoine 2008).

When a particle's energy reaches $E_{sd} = 9.3 \times 10^{19} Z B_{-6} l_{c,-1} \text{ eV}$, the particle enters the semi-diffusive regime with a diffusion coefficient of

$$D_{cl} = \frac{1}{3} c r_L^2 l_c^{-1}. \quad (4)$$

However, most particles have energy much lower than E_{sd} , and thus stay in the diffusive regime. The diffusion coefficient in this regime can be written as (Brunetti & Jones 2014)

$$\begin{aligned} D_{cl} &= \frac{1}{3} \left(\frac{B}{\delta B} \right)^2 c r_L^{2-w} l_c^{w-1} \\ &\approx 6.8 \times 10^{29} \left(\frac{l_c}{0.1 \text{ Mpc}} \right)^{2/3} \left(\frac{E}{1 \text{ GeV}} \right)^{1/3} \\ &\quad \times (B_{-6} Z)^{-1/3} \text{ cm}^2 \text{ s}^{-1}, \end{aligned} \quad (5)$$

where $w = 5/3$ is the spectrum index for Kolmogorov diffusion, $\delta B \sim B$ and $l_0 = l_{0,-1} 0.1 \text{ Mpc}$ are the typical amplitude and scale of magnetic field fluctuations in massive clusters (Brunetti & Jones 2015).

The diffusion time of cosmic rays in the cluster magnetic field can be estimated as

$$t_{\text{diff}} \approx \frac{r_{\text{vir}}^2}{2D_{cl}} = 1.5 M_{15}^{2/3} E_{18}^{-1/3} Z^{1/3} B_{-6}^{1/3} l_{c,-1}^{-2/3} \text{ Gyr}. \quad (6)$$

Cosmic rays with diffusion time longer than the Hubble time $t_H \sim 14 \text{ Gyr}$ would be completely confined by the cluster magnetic field, defining the lower limit of the energy of cosmic rays we expect to observe from the cluster as

$$E_{\text{cr,conf}} = 1.4 \times 10^{15} M_{15}^2 Z l_{0,-1}^{-2} B_{-6} \text{ eV}. \quad (7)$$

Particles with $E > E_{\text{cr,conf}}$ would have a better chance to escape from the cluster magnetic field. To estimate this escape probability, we first write down the probability that a particle with diffusion coefficient D reaches radius r after time t :

$$p(r, t) = \frac{3^{3/2}}{4\pi D t} e^{-3r^2/4Dt} \quad (8)$$

assuming that the particle starts from $r = 0$ and the field is homogenous. The probability that a particle can successfully escape from a cluster of size r_{vir} within the Hubble time is then (Kotera & Lemoine 2008)

$$f_{\text{esc}} \sim \int_{r_{\text{vir}}}^{\infty} dr p(r, t_H) 4\pi r^2 \quad (9)$$

Cosmic rays accelerated in the strong shocks in the accretion region are expected to have a spectrum index $\alpha \sim 2$. The flux of high-energy cosmic rays from a cluster with mass

$M = 10^{15} M_{\odot}$ at redshift $z = 0.1$ can be calculated as

$$\begin{aligned} E_{\text{CR}}^2 \Phi_{\text{CR}} &= E_{\text{CR}}^2 \frac{dN}{dE} \frac{1}{4\pi d_L^2} f_{\text{esc}} (1 - f_{\pi}) \\ &= 0.12 \left(\frac{E}{1 \text{ PeV}} \right)^{2-\alpha} \left(\frac{d_L}{d_L(z=0.1)} \right)^{-2} \\ &\quad \times M_{15}^{1.95} f_{\text{CR},-2} f_{\text{esc}} (1 - f_{\pi}) \text{ eV cm}^{-2} \text{ s}^{-1} \text{ sr}^{-1}, \end{aligned} \quad (10)$$

where d_L is the luminosity distance, and f_{π} is the pion production rate that will be introduced in Section 2.3. Note that we have taken $\alpha \sim 2.1$ in the above estimation. In case of a much softer spectrum, an additional correction term $(\alpha - 2)(\text{PeV/GeV})^{2-\alpha}$ originated from spectrum normalization should be included.

2.3. Neutrino Production

Accelerated cosmic rays would propagate in the cluster magnetic field and interact with both hadron and photon ambience of the ICM. The photon ambience of the ICM includes the Cosmic Microwave Background (CMB) and the intracluster infrared background, but both are subdominant when compared to the hadronic background as shown in Kotera et al. (2009). We thus focus on the hadron background in this work.

The density profile of the thermal gas in the ICM can be described by the classical “ β model” (Cavaliere & Fusco-Femiano 1976):

$$n_{\text{ICM}}(r) = n_{\text{ICM},0} \left[1 + \left(\frac{r}{r_c} \right)^2 \right]^{-3\beta/2}, \quad (11)$$

where $\beta = 0.8$ and $r_c \sim 0.1 r_{\text{vir}}$ is the core radius (Fujita et al. 2003). The density profile is normalized by

$$f_b M = \int \rho_{\text{ICM}}(r) 4\pi r^2 dr, \quad (12)$$

The mass density is related to the number density through $\rho_{\text{ICM}} = n_{\text{ICM}} \mu m_p$, with $\mu \approx 0.61$ being the mean molecular weight.

The magnetic field distribution should trace the baryon distribution in the cluster through the flux conservation $B \propto n_{\text{th}}^{2/3}$ (Brunetti et al. 2004). Specifically, in cluster-sized halos, which we define here to consist of halos greater than $10^{12} M_{\odot}$, the magnetic field as a function of the radial distance from the center of the cluster is given by

$$B(M, r) = B_0 \left(\frac{M}{M_0} \right)^{\lambda} \left[1 + \left(\frac{r}{r_c} \right)^2 \right]^{-\beta} \quad (13)$$

where B_0 is the central magnetic field at a mass of $M_0 = 10^{14} M_{\odot}$, and λ controls the dependence of B_0 on the mass of the cluster in consideration. In our default model, we set $B_0 = 3 \mu\text{G}$ and $\lambda = 0.0$ (Völk & Atoyan 1999; Beck 2012). Following the distribution of n_{ICM} , we define the core radius of the magnetic field model to be equivalent to $r_c = 0.1 r_{\text{vir}}$ and the falloff index $\beta = 0.8$. The magnetic fields in galaxy-sized halos are instead dominated by the dense baryonic cores, and thus have a different structure. We thus use a two part magnetic field model, which adopts the larger of the two following

magnetic fields as in Fang & Linden (2015):

$$B(r) = \max(B_1 e^{-r/R_1}, B_2 e^{-r/R_2}), \quad (14)$$

where $B_1 = 7.6 \mu\text{G}$ and $R_1 = 0.025 R_{\text{vir}}$ and $B_2 = 35 \mu\text{G}$ with $R_2 = 0.008 R_{\text{vir}}$. However, we note that due to the sharp cutoff around R_1 and R_2 , the magnetic field at large radii, where accretion shocks most likely occur, are too low to accelerate to high energies. The contribution from shocks in low-mass halos is rather negligible in our scenario.

For one crossing of the cluster, a particle would expect to confront a column density of

$$\langle y_{\text{ICM}} \rangle \sim \int_0^{r_{\text{vir}}} n_{\text{ICM}}(r) dr = 1.2 \times 10^{22} M_{15}^{0.5} \text{ cm}^{-2}. \quad (15)$$

This corresponds to a pion production rate of

$$f_{\text{pp}} = \langle y_{\text{ICM}} \rangle \sigma_{\text{pp}} \approx 6 \times 10^{-3} M_{15}^{0.5}, \quad (16)$$

where $\sigma_{\text{pp}} \sim 5 \times 10^{-26} \text{ cm}^2$ is the effective proton-proton interaction cross section. Note that particles injected at the cluster center would have a much greater chance to be confined by the cluster magnetic fields, which leads to larger f_{pp} . In contrast, particles injected near the boundary may not even meet an ICM baryon before escaping from the cluster. Since the distribution of baryons in the cluster is not uniform, and different confinement time of particles in the cluster magnetic field would lead to different f_{pp} , in simulations this rate is more precisely calculated by tracking particle propagation in the cluster magnetic field (see Section 3.1).

2.4. Integrated Neutrino Flux

We expect a diffusive neutrino flux integrated from the entire cluster's population. The differential number density, dn/dM , of clusters with mass M at redshift z is given by the halo mass function

$$\frac{dn}{dM}(M, z) = f(\sigma) \frac{\rho_m}{M} \frac{d \ln \sigma^{-1}}{dM}, \quad (17)$$

where ρ_m is the mean density of the universe at the epoch of analysis, $\rho_m(z) = \rho_m(0)(1+z)^3$, and $\sigma(M, z)$ is the rms variance of the linear density field smoothed on a top-hat window function $R = (3M/4\pi\rho_m)^{1/3}$. Specifically, $\sigma^2 = \int dk P^{\text{lin}}(k) \tilde{W}(kR) k^2$, where $\tilde{W}(kR)$ is the Fourier transform of the real-space top-hat window function of radius R (Tinker et al. 2008). For $f(\sigma)$, we adopt the mass function multiplicity described by Sheth & Tormen (1999).

The integrated neutrino flux can be calculated as

$$\begin{aligned} E_\nu^2 \Phi_\nu(E_\nu) &= \int dM \frac{dn}{dM} \frac{(1+z)^2 L_\nu(M, z)}{4\pi d_L^2} \frac{dV}{d\Omega} \\ &= \frac{1}{4\pi} \int_{z_{\text{min}}}^{z_{\text{max}}} \frac{c dz}{H_0 E(z)} \\ &\quad \times \int_{M_{\text{min}}}^{M_{\text{max}}} dM \frac{dn}{dM} E_\nu^2 \frac{dN}{dE} ((1+z)E_\nu, M, z), \end{aligned} \quad (18)$$

where $dV = cdz/(H_0 E(z))(1+z)^2 d_A^2 d\Omega$ is the comoving volume and $d_A = d_L(1+z)^{-2}$ is the angular diameter distance. The lower and upper limits of the integration are taken to be $M_{\text{min}} = 10^{12} M_\odot$ and $M_{\text{max}} = 10^{16} M_\odot$, since galaxies with

$M < M_{\text{min}}$ barely contribute to the energy window we are interested in, while clusters with $M > M_{\text{max}}$ have too low a number density to significantly contribute to the total flux. The redshift integration goes from $z_{\text{min}} = 0.01$, where the closest galaxy clusters are located, up to $z_{\text{max}} = 5$. As we will demonstrate in Section 3.3, the flux from the most distant clusters is dominated by that from the closer ones, so our results are not sensitive to the choice of z_{max} as long as $z_{\text{max}} \gg 1$.

3. RESULTS

3.1. Numerical Setup

The interactions between high-energy protons and ICM baryons were simulated by Monte Carlo as in Fang et al. (2012). The cross sections and products of pp interactions were calculated based on the hadronic interaction model EPOS (Werner et al. 2006). In addition, we implemented the public UHECR propagation code CRPropa3 (Kampert et al. 2013) to study the semi-diffusive propagation of high-energy cosmic rays in cluster magnetic fields.

In our simulation, the baryon distribution in the ICM is set to follow Equation (11). The field is generated to follow the Kolmogorov-type turbulence with spectrum index $w = 5/3$ and have random directions with a coherence length of $l_c \sim 0.03 r_{\text{vir}}$ (Brunetti & Jones 2015). The strength of the magnetic field of the ICM is normalized by Equations (13) and (14). (We will discuss the impact of a stronger or weaker B on our results in Section 4.) Therefore, in our model, the cluster environment is fully determined by two parameters: the cluster mass M and the redshift z .

In the accretion shock scenario, we assume that a stationary shock is located at $d_{\text{sh}} = \lambda_{\text{sh}} R_{\text{ta}}$ (Colafrancesco & Blasi 1998), where $\lambda_{\text{sh}} \approx 0.347$, and $R_{\text{ta}} \approx 2 R_{\text{vir}}$ is the turn-around radius. The maximum energy of the injected cosmic rays is calculated by Equation (2) taking $B = B(d_{\text{sh}})$. Note that adopting the magnetic field strength at the cluster boundary is a conservative assumption as the shocked region in a cluster is not limited to the outer skirts. The injection of cosmic rays is assumed to follow a spectrum $dN/dE \propto E^{-2}$ normalized by Equation (3). The energy fraction f_{cr} is left as a free parameter to be determined by observation.

In the central source scenario, cosmic rays are injected in isotropic directions from the center of the host cluster, with a universal maximum energy $E_{\text{max}} = 50 \text{ PeV}$ and spectrum $dN/dE \propto E^{-1.5}$. The effect of different choices of E_{max} and dN/dE to our results will be discussed in Section 4. Considering that the total luminosity of high-energy sources inside the cluster should scale to the kinetic power of the cluster, we still refer to Equation (3) as the energy budget of injected cosmic rays.

Finally, the diffusive propagation of each particle is tracked until either it successfully leaves the cluster, or its total propagation time exceeds the Hubble time. In the accretion shock scenario, particles are injected isotropically from $d_{\text{sh}} \sim 0.7 R_{\text{vir}}$. Both magnetic field and number density of the ICM are low at the outskirts region, hence some fraction of the particles can leave the cluster within a relatively short time and nearly zero interaction, whereas the others will be trapped toward the inner side of the cluster. In the central source scenario, particles injected from the cluster center confront the densest region of the ICM, and could be easily confined over

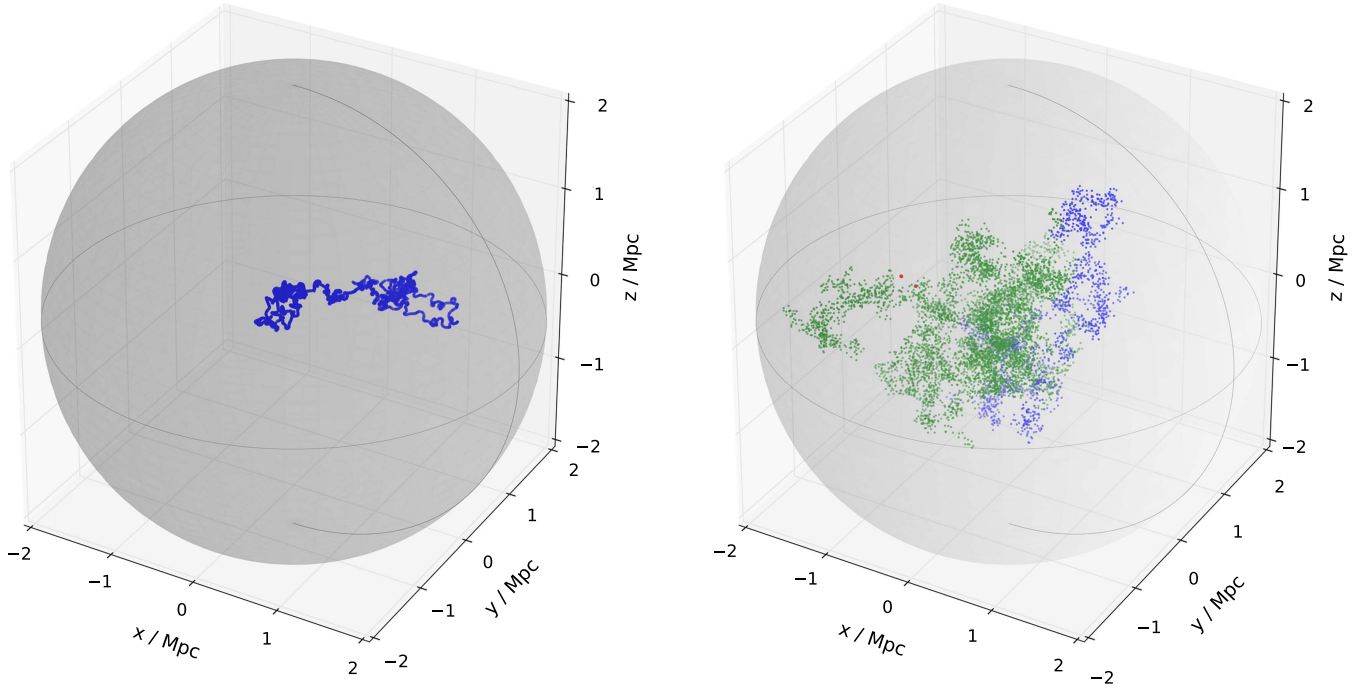


Figure 1. Trajectory of high-energy cosmic rays in the turbulent magnetic field of a model cluster with mass $M = 10^{15} M_{\odot}$ located at redshift $z = 0.1$. The gray sphere represents a cluster. The virial radius of the simulated case is 2.6 Mpc just outside the gray sphere. The baryon and the magnetic field distribution in the ICM follows the “ β model” described by Equations (11) and (13). The central magnetic field strength is $B_0 = 10 \mu\text{G}$. The left panel shows a proton with injection energy $E_p = 10^{19} \text{ eV}$, which has a Larmor radius comparable to the coherence length of the B field. The right panel shows the trajectories of a proton with injection energy $E_p = 10^{17} \text{ eV}$ and its interaction products. The starting point of the proton is at the center of the cluster. The trajectories of the primary proton (blue), the secondary protons (green), as well as the neutron and neutrino products (red) are indicated by a series of points at each propagation step.

the Hubble time. Meanwhile secondary and higher-order protons that resulted from the interactions can lead to further productions of neutrinos (an example of the presence of such secondary particles is shown by the green points in the right panel of Figure 1). The difference of the injection locations leads to quite different behaviors of particles in the two scenarios. The 3d propagation and particle tracking in our simulation are needed to describe the transportation and interaction of particles of all orders in the non-uniform environment, especially when the system is asymmetric as in the accretion shock scenario.

3.2. Cosmic-Ray Trajectories

In this section, we demonstrate the propagation of cosmic rays in the turbulent magnetic field of a model cluster with mass $M = 10^{15} M_{\odot}$ at redshift $z = 0.1$. The central magnetic field strength is set to be $B_0 = 10 \mu\text{G}$. The field strength at the outer skirts is then $B_{\text{vir}} \approx 0.6 \mu\text{G}$. The number density of the ICM gas at the cluster center is $n_0 = 1.1 \times 10^{-2} \text{ cm}^{-3}$, as calculated by Equation (12).

In the left panel of Figure 1, we show the trajectory of a proton with injection energy $E_p = 10^{19} \text{ eV}$. Note that the cluster radius is 2.7 Mpc, though it looks smaller due to the projection of the 3D sphere in the plots. The Larmor radius of the particle is $r_L = 0.01 E_{19} B_0^{-1} \text{ Mpc}$, comparable to the coherence length of the field, which is set to be $l_c = 0.07 \text{ Mpc}$. To study such a semi-diffusive propagation, we utilize the Cash–Karp propagation method of CRPropa to track the particle’s entire trajectory. Each step of the propagation is indicated as a blue point in the plot, and the step size is determined dominantly by the Larmor radius,

because the mean free path of the charged particle is much larger than r_L . As expected, the particle travels almost rectilinearly. In this realization, the particle escaped the cluster without interaction with the ICM gas, and had a total trajectory length of 46 Mpc.

In the right panel of Figure 1, we show the trajectory of a proton with injection energy $E_p = 10^{17} \text{ eV}$. The Larmor radius of the particle is now ~ 700 times less than the coherence length of the field, placing it in the fully diffusive regime. The computing cost for tracking all the steps of the particle would be enormous. Instead, we use the approximation algorithm demonstrated in Kotera & Lemoine (2008). Specifically, taking advantage of the fact that a particle would lose its initial direction after traveling for a distance much longer than the Larmor radius, the particle can be simulated as undergoing a random walk with step size l_c , but each numerical step corresponds to an actual trajectory length $l_c^2/2D$, with D the diffusion coefficient at the particle’s current location. The points in the right panel of Figure 1 hence describe such a random walk with a uniform step size l_c . Note, however, that these steps represent different actual trajectory lengths due to the distinctive D at different parts of the cluster. The blue points correspond to the trajectory of the primary proton, the green ones indicate that of the secondary protons stemming from the interaction with the ICM, and lastly the red ones mark the neutron and neutrino products, including both electron and muon neutrinos. The primary proton was never able to leave the cluster, though the neutrons and some of the secondary protons succeeded. We conclude this section by noting that the trajectories are random and could be very different from realization to realization.

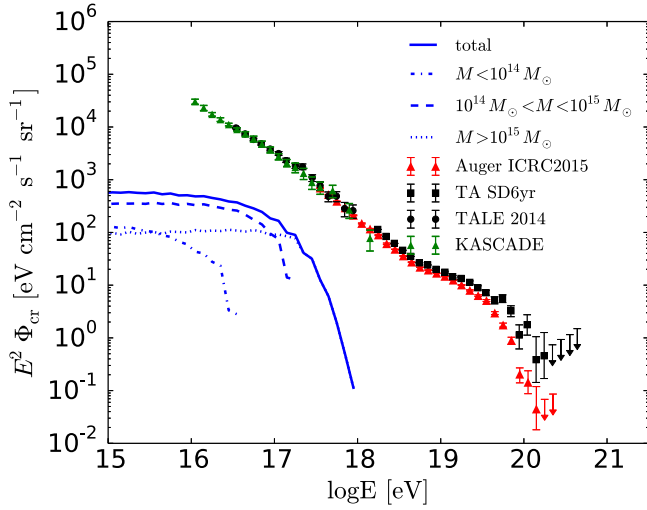


Figure 2. Cumulative cosmic-ray flux from the accretion shocks of galaxy clusters in comparison with observational data from KASCADE (Apel et al. 2013), Auger (Aab et al. 2015), and the Telescope Array (Fukushima 2015). Cosmic-ray protons are injected with a spectrum of $dN/dE \propto E^{-2}$ and a $f_{\text{cr}} = 2\%$ conversion rate from accretion energy to cosmic rays. The solid line indicates the total flux of cosmic rays that escapes the cluster magnetic field within the Hubble time. The contribution is decomposed into three mass groups: $M < 10^{14} M_{\odot}$ (dash-dotted), $10^{14} M_{\odot} < M < 10^{15} M_{\odot}$ (dashed), and $M > 10^{15} M_{\odot}$ (dotted). The central magnetic field strength is assumed to be $3 \mu\text{G}$ for all cluster halos in this scenario.

3.3. Cosmic-Ray and Neutrino Spectra

The integrated cosmic-ray flux from the cluster population in the accretion shock scenario is shown in Figure 2. In all clusters in this scenario, cosmic rays are injected as protons following a power-law spectrum $dN/dE \propto E^{-2}$. The conversion rate from the kinetic energy of the cluster shocks to the cosmic rays is set to be $f_{\text{cr}} = 2\%$ to fit the observed neutrino flux. The turbulent magnetic fields in clusters have a central strength of $B_0 = 3 \mu\text{G}$, and the baryon density of the ICM is scaled to the cluster mass by $n_0 \propto f_b \propto M^{0.16}$. The solid line indicates the flux of the cosmic rays that could successfully leave the clusters and be observed at the Earth. The overall spectrum follows E^{-2} as the injection spectrum and is cut off around $10^{17.5} \text{ eV}$. The contribution to cosmic-ray flux from clusters is subdominant in all energies comparing to observation. The integrated cosmic-ray flux in the central source scenario has a similar behavior as in the accretion shock scenario, except that we assume the flux follows a $E^{-1.5}$ injection spectrum.

We further decompose the flux into the contribution from three mass groups: $M < 10^{14} M_{\odot}$, $10^{14} M_{\odot} < M < 10^{15} M_{\odot}$, and $M > 10^{15} M_{\odot}$, shown in dash-dotted, dashed, and dotted lines correspondingly. Because the cosmic-ray luminosity significantly depends on the cluster mass through $L_{\text{cr}} \propto M^{1.95}$, clusters below $10^{14} M_{\odot}$ are not as luminous as the massive clusters. In addition, since $E_{\text{max}} \propto M^{2/3}$, particles from these clusters cannot reach the highest energies. However, since the strength and scale of magnetic fields in these clusters are also smaller, particles have a better chance to leave the source. The combined impact of these factors leads to a contribution of this mass group to $\sim 1/3$ of the total cosmic-ray flux around PeV, and $\leq 10\%$ above 10^{17} eV . The $10^{14} M_{\odot} < M < 10^{15} M_{\odot}$ group is found to make the largest contribution to the flux up to the ankle around 10^{18} eV .

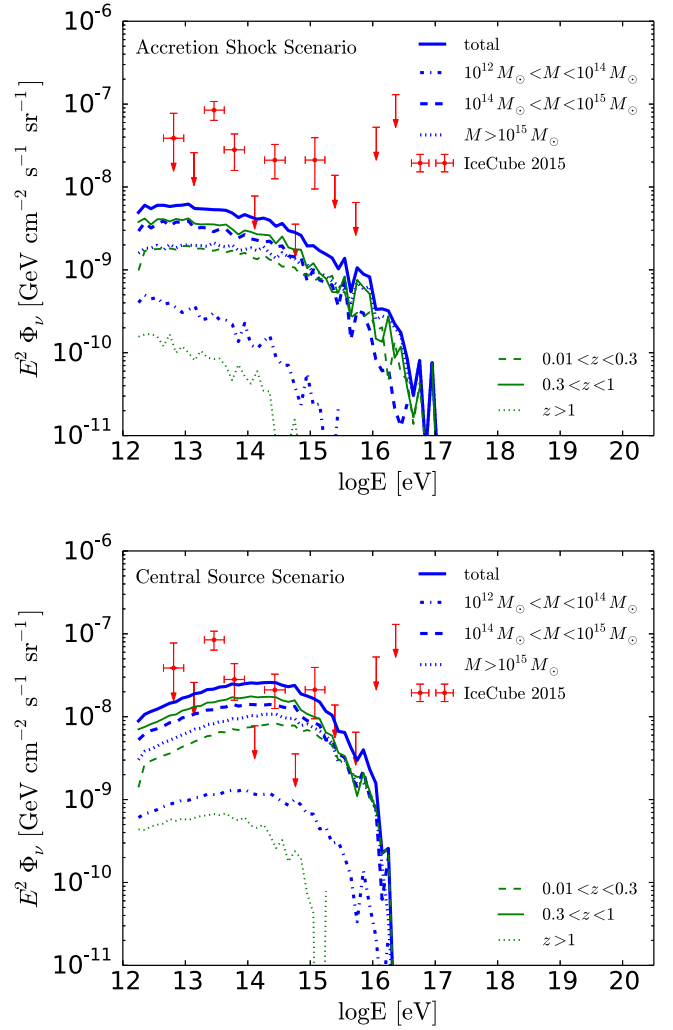


Figure 3. Cumulative neutrino flux from the galaxy clusters compared to the IceCube observations (Aartsen et al. 2015). Top: accretion shock scenario: as in Figure 2, the cosmic-ray injection follows $dN/dE \propto E^{-2}$, $f_{\text{cr}} = 2\%$, and a maximum energy following Equation (2), determined by particle acceleration and escape in the accretion shocks. Bottom: central source scenario: the cosmic-ray injection follows $dN/dE \propto E^{-1.5}$, $f_{\text{cr}} = 0.5\%$, and $E_{\text{max}} = 5 \times 10^{16} \text{ eV}$. The blue thin lines decompose the contribution into three mass groups: $M < 10^{14} M_{\odot}$ (dash-dotted), $10^{14} M_{\odot} < M < 10^{15} M_{\odot}$ (dashed), and $M > 10^{15} M_{\odot}$ (dotted). The green thin lines instead decompose the flux into three redshift bins: $0.01 < z < 0.3$ (dashed), $0.3 < z < 1$ (solid), and $z > 1$ (dotted).

Above the ankle, clusters with mass $M > 10^{15} M_{\odot}$ are needed to produce UHE protons. However, due to the exponential cutoff in the halo mass function for such extremely massive clusters, a significant production of UHECRs from clusters is not found given a pure proton injection. The main contribution of this proton component is relevant to explain the second knee observed around 10^{17} eV (Apel et al. 2013). Heavier nuclei, if injected at the shocks, may reach ultra-high energies, but their neutrino production would be less significant.

As displayed in Figure 1, within the same cluster, cosmic rays with lower energy have a lower chance of leaving the system due to their smaller Larmor radius. Consequently, the spectrum of the escaped cosmic rays is slightly harder than that at injection.

The cumulative neutrino flux from clusters is shown in Figure 3. The top panel corresponds to the accretion shock scenario. The injection of cosmic rays and the cluster environment are set up as in Figure 2. The total neutrino flux is indicated by the solid blue line. With $f_{\text{cr}} = 2\%$, clusters contribute a neutrino flux less than 20% of the IceCube detections. Unlike the cosmic-ray spectrum, which mainly scales with the escape probability f_{esc} , the neutrino spectrum is rather sensitive to the pion production rate f_{π} . The spectral index is found to be about two around TeV, 2.4 at PeV and cut off above 10 PeV. The spectrum softening at PeV is a combined effect of diffusion (lower f_{π} at higher energies) and cluster mass function (higher flux but lower rate for massive clusters).

The bottom panel of Figure 3 shows the integrated neutrino flux in the central source scenario. The spectrum below ~ 100 TeV is mainly determined by the injection and thus follows $\sim E^{-1.5}$. Interestingly, at higher energies the softening effect due to the shorter cosmic-ray diffusion time and the lower population of massive clusters dominates over the hard injection. As a result, with $f_{\text{cr}} = 0.5\%$ this scenario could reproduce the spectrum and flux of the IceCube measurement above ~ 30 TeV.

As in Figure 2, we also decompose the neutrino contribution into three mass groups: $M < 10^{14} M_{\odot}$ (dash-dotted), $10^{14} M_{\odot} < M < 10^{15} M_{\odot}$ (dashed), and $M > 10^{15} M_{\odot}$ (dotted), all indicated by blue lines. The significance of the three mass groups' contribution to the neutrino fluxes follows a similar order as that of cosmic rays, except that without the f_{esc} factor impacting the neutrino production, the $M < 10^{14} M_{\odot}$ group now contributes less than 5% of the total flux. The thin green lines in Figure 2 decompose the contribution into three redshift bins: $0.01 < z < 0.3$ (dashed), $0.3 < z < 1$ (solid), and $z > 1$ (dotted). We find that due to the intense source distribution in the region $0.3 < z < 1$, this group makes the largest contribution to neutrino production. Due to the distance and the rare rate of massive clusters at high redshift, clusters at $z > 1$ barely contribute.

4. DISCUSSION AND CONCLUSION

Unlike other astrophysical sources, galaxy clusters offer a unique environment for TeV–PeV neutrino production through efficient acceleration and confinement of high-energy cosmic rays. By propagating particles in three-dimensional turbulent magnetic fields and recording their interactions with the ICM gas, we find that the integrated neutrino flux from the cluster accretion shocks could account for $\leq 20\%$ of the IceCube detections, while neutrinos produced by the interaction of cosmic rays from powerful sources hosted by clusters could explain both the flux and spectrum of the IceCube data above 30 TeV, if the injection spectrum is harder than two. The lack of neutrino clustering around known sources also fits well with the cluster production model. In addition, the high-energy cosmic rays that succeed in escaping from the clusters contribute less than 20% of the observed cosmic-ray flux around and below the ankle, and may explain the second knee feature when galactic and ultra-high-energy cosmic-ray accelerators' contributions are added to the clusters' contribution.

Our results demonstrate that when taking into account the effect of cosmic-ray confinement and the mass dependence of the cluster number density, the integrated neutrino spectrum would conserve the injection spectrum around TeV–100 TeV,

but become much steeper above PeV. If high-energy sources harbored in the galaxy clusters could produce cosmic rays with spectra harder than E^{-2} , the tension between the neutrino-associated GeV γ rays and the *Fermi* measurement of isotropic diffusive γ -ray background (Ackermann et al. 2015; Murase et al. 2016) can be alleviated. Also notice that in the cluster scenario, the dominant contribution comes from sources beyond $z \sim 0.3$ (as suggested by Figure 3). Thus, γ rays with $E \gtrsim 0.1$ TeV are attenuated by the time they arrive on Earth, through interactions with photons of the extragalactic background light (EBL) and the CMB that have a non-trivial optical depth, $\tau_{\gamma\gamma}(z \sim 0.3) > 1$ (Stecker et al. 2006).

The search for the first γ rays from galaxy clusters is still ongoing. No significant spatially extended γ -ray emission from the nearby galaxy clusters was found in four years of *Fermi*-LAT data, establishing limits on the cosmic ray to thermal pressure ratio, X_{CR} , to be below 1.4% (Ackermann et al. 2014). The parameter f_{CR} of our model can be translated to X_{CR} by $X_{\text{CR}} = P_{\text{CR}}/P_{\text{th}} \sim 0.6\% f_{\text{CR},-2} (\dot{M} t_{\text{cr,conf}}/M)$, where $P_{\text{CR}} \approx (1/3)f_{\text{CR}}(GM\rho_{\text{ICM}} t_{\text{cr,conf}}/r_{\text{vir}})$ is the cosmic-ray pressure after an accumulation of particles for $t_{\text{cr,conf}}$, and $P_{\text{th}} = n_{\text{ICM}}(GM\mu_p/2 r_{\text{vir}})$ is the thermal pressure. The $f_{\text{CR}} < 2\%$ suggested by our model is thus consistent with the constraint from γ -ray searches. However, the *Fermi* limit would constrain cluster scenarios with $f_{\text{CR}} > 2\%$, corresponding to an injection index $\alpha > 2.1$.

In the central source scenario (bottom panel of Figure 3), we showed a benchmark case with an injection spectrum index of $\alpha = 1.5$ and maximum cosmic-ray energy $E_{\text{max}} = 50$ PeV. The results are solid under moderate adjustments on either α or E_{max} (including adding a mass dependence). However, α cannot be as large as ~ 2 , otherwise the γ -ray counterpart will clearly exceed the *Fermi* measurements of the isotropic γ -ray background. Furthermore, if $E_{\text{max}} \ll 50$ PeV, the injected cosmic rays would not be energetic enough to produce the PeV neutrinos. On the other hand, if $E_{\text{max}} \gg 50$ PeV in all clusters, the resulting neutrino spectrum could overshoot the null bins at 5–10 PeV.

In our simulations, we assumed a central magnetic field strength of $3 \mu\text{G}$. In the case of a smaller central magnetic field strength B_0 , the highest energy cosmic rays would have a higher chance to leave the system due to the weaker magnetic field and less interaction materials in the environment. Lower energy cosmic rays would be less impacted, since they are confined to a relatively small volume. Hence, the overall neutrino spectrum would be expected to have a lower flux but a softer spectrum. Conversely, stronger B_0 would lead to a higher neutrino flux due to the intenser confinement.

Neither of our scenarios could account for the IceCube data below 30 TeV. Although the majority of the neutrinos are expected to come from extragalactic sources, Galactic sources could potentially contribute some fraction of the flux (Ahlers et al. 2016), especially below ~ 200 TeV (Murase 2015). It is also possible that other types of sources could contribute to this energy range.

Our conclusion on the accretion shock scenario is consistent with that from Zandanel et al. (2015), though the two works have distinctive approaches. While Zandanel et al. (2015) derived the neutrino luminosity from a scaling between radio and gamma-ray luminosities, we directly simulated the particle propagation to obtain the neutrino spectrum. Zandanel et al. (2015) did not assume any cosmic-ray spectral steepening due

to the escape of high-energy cosmic rays, whereas in our work this cutoff was shown as a natural result from the energy-dependent transportation, and crucial for the survival of the central source scenario. On the other hand, Zandanel et al. (2014, 2015) indicated that the neutrino contribution from clusters could be further limited due to the fact that not all clusters are expected to produce hadronic emissions. The same constraint could also apply to our results in the accretion shock scenario.

Although consistent with current γ -ray and radio detection limits, the cluster scenario could be robustly tested by the growing statistics of IceCube as well as γ -ray searches of galaxy clusters in the near future. If the cluster contribution to the diffusive γ -ray background and the cosmic ray to thermal pressure ratio can be further constrained by the γ -ray observations, a significant contribution to IceCube neutrinos from galaxy clusters would be ruled out. On the other hand, because our model predicts a dominant neutrino flux from the most massive clusters above ~ 5 PeV, the future detection of strong anisotropy in this energy regime would provide firm support to the cluster scenario.

We thank Cole Miller and Kohta Murase for helpful discussions. K.F. acknowledges the support of a Joint Space-Science Institute prize postdoctoral fellowship. A.O. acknowledge financial support from the NSF grant NSF PHY-1412261 and the NASA grant 11-APRA-0066 at the University of Chicago, and the grant NSF PHY-1125897 at the Kavli Institute for Cosmological Physics. This work made use of computing resources and support provided by the Research Computing Center at the University of Chicago.

REFERENCES

- Aab, A., Abreu, P., Aglietta, M., et al. 2015, Proc. ICRC
- Aartsen, M. G., Abbasi, R., Abdou, Y., et al. 2013a, *Sci*, 342, 1242856
- Aartsen, M. G., Abbasi, R., Abdou, Y., et al. 2013b, *PhRvL*, 111, 021103
- Aartsen, M. G., Abbasi, R., Abdou, Y., et al. 2013c, *ApJ*, 779, 132
- Aartsen, M. G., Ackermann, M., Adams, J., et al. 2015, *PhRvD*, 91, 022001
- Aartsen, M. G., Ackermann, M., Adams, J., et al. 2015, *Aph*, 66, 39
- Ackermann, M., Ajello, M., Albert, A., et al. 2014, *ApJ*, 787, 18
- Ackermann, M., Ajello, M., Albert, A., et al. 2015, *ApJ*, 799, 86
- Ahlers, M., Bai, Y., Barger, V., & Lu, R. 2016, *PhRvD*, 93, 013009
- Ahlers, M., & Halzen, F. 2014, *PhRvD*, 90, 043005
- Apel, W. D., Arteaga-Velázquez, J. C., Bekk, K., et al. 2013, *Aph*, 47, 54
- Arons, J. 2003, *ApJ*, 589, 871
- Bechtol, K., Ahlers, M., Di Mauro, M., Ajello, M., & Vandenbroucke, J. 2015, arXiv:1511.00688
- Beck, R. 2012, *SSRv*, 166, 215
- Berezinsky, V. S., Blasi, P., & Ptuskin, V. S. 1997, *ApJ*, 487, 529
- Blasi, P., Epstein, R. I., & Olinto, A. V. 2000, *ApJL*, 533, L123
- Brunetti, G., Blasi, P., Cassano, R., & Gabici, S. 2004, *MNRAS*, 350, 1174
- Brunetti, G., & Jones, T. W. 2014, *IJMPD*, 23, 1430007
- Brunetti, G., & Jones, T. W. 2015, in *Astrophysics and Space Science Library*, Vol. 407, ed. A. Lazarian, E. M. de Gouveia Dal Pino, & C. Melioli, (Berlin Heidelberg: Springer), 557
- Cavaliere, A., & Fusco-Femiano, R. 1976, *A&A*, 49, 137
- Colafrancesco, S., & Blasi, P. 1998, *Aph*, 9, 227
- Dar, A., & Shaviv, N. J. 1995, *PhRvL*, 75, 3052
- de Marco, D., Hansen, P., Stanev, T., & Blasi, P. 2006, *PhRvD*, 73, 043004
- Dermer, C. D., Murase, K., & Inoue, Y. 2014, arXiv:1406.2633
- Dermer, C. D., Murase, K., & Takami, H. 2012, *ApJ*, 755, 147
- Fang, K., Kotera, K., Murase, K., & Olinto, A. V. 2013, arXiv:1311.2044
- Fang, K., Kotera, K., & Olinto, A. V. 2012, *ApJ*, 750, 118
- Fang, K., & Linden, T. 2015, *PhRvD*, 91, 083501
- Fang, K., & Miller, M. C. 2016, *ApJ*, 826, 102
- Farrar, G. R., & Gruzinov, A. 2009, *ApJ*, 693, 329
- Fujita, Y., Takizawa, M., & Sarazin, C. L. 2003, *ApJ*, 584, 190
- Fukushima, M. 2015, in EPJ Web Conf., Proceedings, 18th International Symposium on Very High Energy Cosmic Ray Interactions (ISVHECRI 2014), CERN (August 18th-22nd, 2014), 99, 04004
- Gonzalez, A. H., Sivanandam, S., Zabludoff, A. I., & Zaritsky, D. 2013, *ApJ*, 778, 14
- Guo, F., Li, H., Daughton, W., & Liu, Y.-H. 2014, *PhRvL*, 113, 155005
- Hong, S. E., Ryu, D., Kang, H., & Cen, R. 2014, *ApJ*, 785, 133
- Hu, W., & Kravtsov, A. V. 2003, *ApJ*, 584, 702
- Inoue, S., Sigl, G., Miniati, F., & Armengaud, E. 2007, arXiv:astro-ph/0701167
- Jokipii, J. R. 1987, *ApJ*, 313, 842
- Kampert, K.-H., Kulbartz, J., Maccione, L., et al. 2013, *Aph*, 42, 41
- Kang, H., Rachen, J. P., & Biermann, P. L. 1997, *MNRAS*, 286, 257
- Kotera, K., Allard, D., Murase, K., et al. 2009, *ApJ*, 707, 370
- Kotera, K., & Lemoine, M. 2008, *PhRvD*, 77, 023005
- McBride, J., Fakhouri, O., & Ma, C.-P. 2009, *MNRAS*, 398, 1858
- Mészáros, P. 2006, *RPPh*, 69, 2259
- Miniati, F. 2015, *ApJ*, 800, 60
- Miniati, F., Ryu, D., Kang, H., et al. 2000, *ApJ*, 542, 608
- Murase, K. 2015, in AIP Conf. Proc., 26th International Conference on Neutrino Physics and Astrophysics (Neutrino 2014), 1666 (Melville, NY: AIP), 040006
- Murase, K., Ahlers, M., & Lacki, B. C. 2013, *PhRvD*, 88, 121301
- Murase, K., Dermer, C. D., Takami, H., & Migliori, G. 2012, *ApJ*, 749, 63
- Murase, K., Guetta, D., & Ahlers, M. 2016, *PhRvL*, 116, 071101
- Murase, K., Inoue, S., & Nagataki, S. 2008, *ApJL*, 689, L105
- Murase, K., Inoue, Y., & Dermer, C. D. 2014, *PhRvD*, 90, 023007
- Murase, K., Mészáros, P., & Zhang, B. 2009, *PhRvD*, 79, 103001
- Planck Collaboration, Ade, P. A. R., Aghanim, N., et al. 2015, arXiv:1502.01589
- Rordorf, C., Grasso, D., & Dolag, K. 2004, *Aph*, 22, 167
- Ryu, D., Kang, H., Hallman, E., & Jones, T. 2003, *ApJ*, 593, 599
- Sheth, R. K., & Tormen, G. 1999, *MNRAS*, 308, 119
- Stecker, F. W., Done, C., Salamon, M. H., & Sommers, P. 1991, *PhRvL*, 66, 2697
- Stecker, F. W., Malkan, M. A., & Scully, S. T. 2006, *ApJ*, 648, 774
- Tinker, J., Kravtsov, A. V., Klypin, A., et al. 2008, *ApJ*, 688, 709
- Vazza, F., Gheller, C., & Brüggén, M. 2014, *MNRAS*, 439, 2662
- Völk, H. J., Aharonian, F. A., & Breitschwerdt, D. 1996, *SSRv*, 75, 279
- Völk, H. J., & Atoyan, A. M. 1999, *Aph*, 11, 73
- Werner, K., Liu, F.-M., & Pierog, T. 2006, *PhRvC*, 74, 044902
- Winter, W. 2013, *PhRvD*, 88, 083007
- Wolfe, B., Melia, F., Crocker, R. M., & Volkas, R. R. 2008, *ApJ*, 687, 193
- Zandanel, F., Pfrommer, C., & Prada, F. 2014, *MNRAS*, 438, 124
- Zandanel, F., Tamborra, I., Gabici, S., & Ando, S. 2015, *A&A*, 578, A32